Hydrodynamic forces on an oblate spheroid in contact with a smooth surface in a linear shear flow

Enzo de Souza, Rafik Ouchene, Lionel Thomas

Hydrodynamic forces on an oblate spheroid in contact with a smooth surface in a linear shear flow

Enzo De Souza,[1] Rafik Ouchene,[1, a)] and Lionel Thomas[1]
CNRS, Institut Pprime, UPR 3346, 11 Boulevard Marie et Pierre Curie, Site du futuroscope, 86073 Poitiers, France

In this work, a computational fluid dynamics of a linear shear flow past an oblate spheroid resting on a surface was conducted. The present study aims to compute the hydrodynamic forces experienced by oblate spheroids in contact with a smooth surface. Using the computational results, we derive correlations for the hydrodynamic drag, lift, and drift coefficients. These correlations are provided for an aspect ratio ranging from 0.2 to 1, for particle Reynolds numbers up to 7. In addition, it is found that the Stokesian evolution of the drag coefficient as a function of the orientation remains valid in the considered configuration; that is, the drag coefficient evolves as a so-called "square-sine" profile. Surprisingly, it was found that the lift induced by shear was also found to evolve as "square-sine" with respect to the spheroid orientation. Furthermore, we found that the drift coefficient evolves as a so-called "cosine-sine" profile with respect to the spheroid orientation.

Keywords: Drag, Lift, Oblate spheroid Shear flow

I. INTRODUCTION

Understanding the complex aero- or hydro-dynamic forces acting on non-spherical particles resting on a surface is of great importance in numerous environmental and industrial applications where particle re-suspension occurs. Transport of sediment grains in a river[1], pollutants transport in rivers[2], transport of sand by wind[3], pollutant dispersion in the environment[4], pollen transport[5], incipient motion of particle from substrate[6], particle aggregation in combustion aerosols[7,8], or contamination in a microelectronics industry[9], among others, are the areas in which knowledge of the forces involved in particle re-suspension plays a critical role. In practice, particles in such processes can have an indefinite possibility of sizes and shapes that are more often irregular[10]. The intricate way in which non-spherical particles interact with the flow motivates studies of the shape effect on particle transport and, accordingly, involves the opening investigation of the hydrodynamic forces acting on non-spherical particles. Nowadays, the modeling of such processes using the Euler-Lagrange approach is more and more moving towards non-spherical particles to take into account the significant effect of the particle shape as opposed to the common use of perfectly spherical particles[11–19]. From a practical point of view, the indefinite possibility of non-spherical shapes are approximated by some regular geometries such as spheroids and cylinders. However, although the particle shapes are approximated by these regular geometries, a complete description of the behavior of these particles requires the modeling of the hydrodynamic forces acting on the particle, taking its orientation into account, as opposed to the spherical particle case. In the past decades, hydrodynamic forces acting on non-spherical particles have received numerous investigations[20–30] which were mainly devoted to the non-spherical particles away from the surface. Thus, their use is neither accurate nor adequate in the context of re-suspension, where the presence of a surface can significantly affect the hydrodynamic forces. This compact literature overview is meant to illustrate the relevance of investigating hydrodynamic forces on non-spherical particles, but for the sake of brevity and clarity, details are not recalled. Interested readers are referred to the reviews of the techniques describing the motion of non-spherical particles, and also the numerical and experimental methods used for measuring particle dynamics produced by Voth & Soldati[31]. The readers can also refer to the recent extensive review by Michaelides and Feng[32] on drag coefficients of non-spherical particles. The authors of the study examined the state of knowledge of the drag coefficients of non-spherical particles based on a review of the available correlations in the literature. General recommendations are proposed by the authors on the use of these correlations in the numerical simulations.

And still, despite the numerous works carried out to quantify the impact of non-spherical shapes on the hydrodynamic forces, they are unfortunately limited when employed in the specific context of re-suspension, where the presence of a surface affects substantially these hydrodynamic forces. Moreover, particles resting on a surface in a fluid flow are unfortunately less investigated, thus requiring significant efforts to predict the hydrodynamic forces in such a condition.

Many researchers have investigated particle motion in a slow shear flow[33–37]. Saffman[33] demonstrates that a sphere moving with a certain velocity in a very viscous liquid, relative to a simple shear flow, experiences a lift force perpendicular to the flow. However, the derived results are known to be compromised as the sphere approches the wall. Goldman et al.[36] derived asymptotic solutions for the Stokes equations to describe the transla-

[a)] Electronic mail: r.ouchene1@gmail.com

tional and rotational motion of a sphere close to a plane wall in a viscous fluid, particularly as the gap between the sphere and wall narrows. The issue of a linear shear flow over a fixed spherical particle in contact with a smooth surface was considered by O'Neill[38] who derived an exact solution to the linearised Stokes flow equations. The values of the hydrodynamic force and pitching torque acting on a sphere are determined explicitly. Similarly, Leighton & Acrivos[37] determined the lift force on a stationary sphere on a smooth plane when placed in a simple shear flow under conditions of small Reynolds numbers ($Re_p < 1$). Particularly, the authors showed that the ratio between the lift and drag forces is of $0.114Re_p$, which indicates that the lift force is negligible at low particle Reynolds number. For the purpose of examining the hydrodynamic forces acting on a finite-sized spherical particle moving in a wall-bounded shear flow, Zeng et al.[39] performed numerical simulations for a limiting case of a stationary spherical particle in a wall-bounded shear flow at a finite Reynolds number and varying distances from the wall. Particular attention was paid to a spherical particle in contact with a smooth wall. The authors provided correlations for both drag and lift coefficients that are valid in a wide range of particle Reynolds number $Re_p < 250$.

As far as we are aware, only a few works dealing with the hydrodynamic forces experienced by non-spherical particles resting on a surface are reported in the literature.

Wakiya[34] provides analytical results for a spheroid in the Couette flow, where the steady translation of one of the two walls drives the flow presenting a case for the analytical value of drag and torque acting on a spheroid fixed in a shear flow depending of distance to wall. A constant can be determined in the case of Couette shear flow to be about 1.67 for drag force which remains vastly different from constant found by Goldman et al.[36] and O'Neill[38]. Price[40] examines a three-dimensional Stokes flow where a hemispherical bump is introduced into shear flow along a plane wall. The disturbance flow around the bump is calculated, revealing a recirculatory motion near the base of the hemisphere. Additionally, the force and torque exerted on the bump were determined. El-Kareh & Secomb[41] analysed axisymmetric Stokes flow impacting a spherical cap on a solid plane wall. The study provided the pressure distribution and axial force on caps of various shapes, showing that axial force is proportional to cap volume but less sensitive to shape flattening for a fixed volume. Sugiyama & Sbragaglia[42] further investigates three-dimensional shear flow over a hemispherical droplet on a plane wall, with solutions depending on the viscosity ratio between the droplet and surrounding fluid. It extends Price's earlier work on no-slip hemispherical bumps. Key results include expressions for the torque and force on the droplet and the effect of surface deformations at low capillary numbers. Martino et al.[43] experimentally examines the onset of motion for a partially exposed cylinder in a shear flow within a narrow channel. Positioned perpendicular to the flow in a test zone, the cylinder's varying exposure to the flow simulates the effects of sediment bed constraints in natural sediment transport. The study highlights the relationship between particle mobility at critical conditions and the degree of burial, showing how exposure and mechanical resistance, defined by the static pivot angle, impact the cylinder's movement. Boulbene et al.[44] performed numerical simulations of the laminar shear flow past a bacterial cell attached to a plane surface. To clarify the prevailing mechanisms involved in the detachment of model bacteria, the authors computed the induced hydrodynamic forces and torque exerted on the cell. The focus was on the prolate spheroids with an aspect ratio ranging from 1 to 2 and orientation in the interval of $[0 - \pi/2]$ in the Stokes regime flow. Particularly, from the discussion of the drag and torque magnitude with respect to the cell orientation, it was shown that reorientation and rolling of spheroid-shaped cells are favored. On the other hand, they found that rod-shaped cells tend to lie on the surface and align with the flow direction. By applying a resolved discrete particle method, Musong et al.[45] studied the drag force on non-spherical (rod and cone) particles in contact with a wall. They noticed that the particle's shape or orientation has a significant effect on the drag force. In addition, the authors observed that particle-wall separations as well as their length significantly affect the drag force. To examine the mobilisation of bacteria in turbulent wind conditions Brambilla et al.[46], review the understanding of the forces for colloidal spherical particles and extends the existing theories to rod-shaped particles. The authors re-derived the equations for the drag and lift forces accounting for the shape of the particle. Fillingham et al.[47] conducted Direct numerical simulations of a steady flow over an isolated prolate spheroid of revolution resting on a surface parallel to their long axis. Four aspect ratios (1.5, 2, 3 and 5) were considered in addition to the spherical case, while the particle Reynolds number was taken up to 10. Thanks to the results of the simulations, the authors provided correlations for drag, lift, and torque coefficients, taking the aspect ratio, the particle Reynolds number, and the particle orientation into account. Ting et al.[48] evaluated the drag and lift forces acting on oblate spheroids on a smooth solid surface using a numerical simulation of Couette linear shear flow over these particles. The special cases of interest in their investigation were the oblate spheroids of revolution with their short axis perpendicular to the surface and aspect ratios of 0.025, 0.05, 0.1, 0.25, 0.5, and 1 in a Stokes regime flow. As a main result, these authors introduced shape-dependent corrections into traditional Stokes formulae for spherical particles[49]. More recently, a numerical study of the hydrodynamic force exerted on a prolate hemispheroidal particle attached to a smooth surface has been performed by Naghashnejad et al.[50]. Using their computational results, the authors provided a correlation for the drag coefficient as a function of more general descriptors of the geometry commonly used in the case of

particles with irregular shapes. Three aspect ratios were considered (1, 3, and 5) at only one particle Reynolds number, $Re_p = 10$, while two orientations were considered, namely, the pitch angle with respect to the surface and the orientation angle with respect to the flow direction. The commercial code "COMSOL Multiphysics" has been used by Baghat and Goswami[51] to perform numerical simulations of a linear shear flow past a prolate spheroid in the vicinity of a rough wall. The focus was on the estimation of the hydrodynamic forces and torque at different wall separation distances and inclination angles. By making use of their computational results, the authors provide the correlations for the drag and lift coefficients to describe the effect of rough surface, inclination angles, and particle Reynolds numbers. In a recent paper by Chéron et al.[52], an investigation of a linear shear flow past a rod-like (spherocylinder) particle has been conducted by a direct numerical simulation carried out with an immersed boundary method. The computational data, in combination with the available expressions in the viscous regime, are used to derive new correlations for drag, lift, and torque coefficients for various fluid flow regimes and velocity profiles, including locally uniform flow and locally linear shear flow. Following this investigation, Chéron & van Wachem[53] presents novel correlations to predict the drag, lift, and torque coefficients of axi-symmetric rod-like particles in wall-bounded linear shear flow. In this study the particle position and particle orientation with respect to the wall are varied in view of analysing its influence on hydrodynamic forces. The authors provided new correlations depending on the particle Reynolds number, orientation angle, aspect ratio, and the dimensionless distance to the wall. Wall effects are modeled as a multiplication factor for drag and additional contributions for lift and torque. They further took into account particle wall distance providing a variety of correlations for different regimes using Zeng et al.[39] and provided an analysis on wall effect on drag, lift and torque for rod-like particle. Lain et al.[54] investigated by numerical simulation the influence of simple shear flow on resistance coefficients. Three particles shape, namely, prolate and oblate ellipsoids and cylinders, were considered at particle Reynolds numbers of $Re_p = 1$, 10 and 100 at only the pitch angle,$\phi_p \in [0^o - 180^o]$, in addition to the fluid spin ratio. Their physical analysis was focused on the pressure and frictional contribution to the hydrodynamic forces and pitching torque. Especially, one of their main findings is that the pressure and frictional drag coefficients are independent of the shear flow. However, referring to Chéron et al.[52], there may exist an apparent difference in shear flow cases where the flow speed is perpendicular to the axis of symmetry because the non-uniform effect of shear flow may rotate the particle. Despite the wide range of parameters analysed by Lain et al.[54], the effect of wall contact and the orientation angle are, unfortunately, not investigated in their study.

From the investigations recounted in the previous paragraphs, it is clearly noticeable that the present issue has recently received more interest from researchers and further efforts are needed to design new correlations for the hydrodynamic coefficients, aiming at accounting for the non-spherical particles resting on a surface. The spheroidal shape of the particle seems to be a special case of interest since it allows describing both elongated (prolate) and flattened (oblate) particles. As discussed herein before, Fillingham et al.[47] investigated the case of prolate spheroids resting on a plane. The present work is therefore undertaken with the aim of developing accurate and simple correlations for the drag, lift, and drift forces acting on an isolated oblate spheroid resting on a smooth plane. The investigation is conducted for an aspect ratio ranging from 0.2 to 1, for a particle Reynolds number up to 7, for an orientation angle $\phi_f \in [0^o - 90^o]$ and for a pitch angle of $\phi_f = 0^o$. Accordingly, computational fluid dynamics in this configuration were conducted using a body-fitted numerical method for acquiring a wide database of these hydrodynamic coefficients and used to reach this objective.

The rest of this document is organized as follows. The problem is first formulated and conceptualized in a sketch in Section 2. In Section 3, the computational methodology is thoroughly described, along with the validation cases. The flow visualization and the computational results are given before introducing the provided correlations in Section 4. Finally, Section 5 is devoted to summarizing our findings and discussing the possible perspectives.

II. PROBLEM FORMULATION

In this work, we follow the same approach used by Fillingham et al.[47] for the prolate spheroids, extending this choice to the oblate spheroids. Thus, we consider an isolated oblate spheroidal particle attached to a smooth plane whose axis of symmetry is parallel to the plane. It should be emphasized that, throughout the rest of the document, this will be called spheroid-on-a-smooth-surface. A schematic of the flow configuration, spheroid position, and orientation is shown in Figure 1. Particles are characterized by dimensionless parameters. The dimensionless shape factor is the aspect ratio, defined as the ratio between the revolution axis and the major axis $\lambda = \frac{b}{a}$. The flow orientation angle, ϕ_f, is the angle between the revolution axis and the flow direction, whereas the particle pitch angle, ϕ_p, is the angle between the revolution axis with respects to the surface ($xy-plane$). The volume equivalent spherical diameter, $d_p = [6V_p/\pi]^{1/3}$, taken to be the relevant characteristic length scale. Here, $V_p = \frac{4}{3}\pi b\, a^2$ is the volume of the considered spheroid. As the hydrodynamic coefficients depend on the flow around the spheroid, the particle Reynolds number at which the hydrodynamic coefficients is commonly defined as:

$$Re_p = \frac{U_c d_p}{\nu} = \frac{2\gamma a^2 \lambda^{1/3}}{\nu} \tag{1}$$

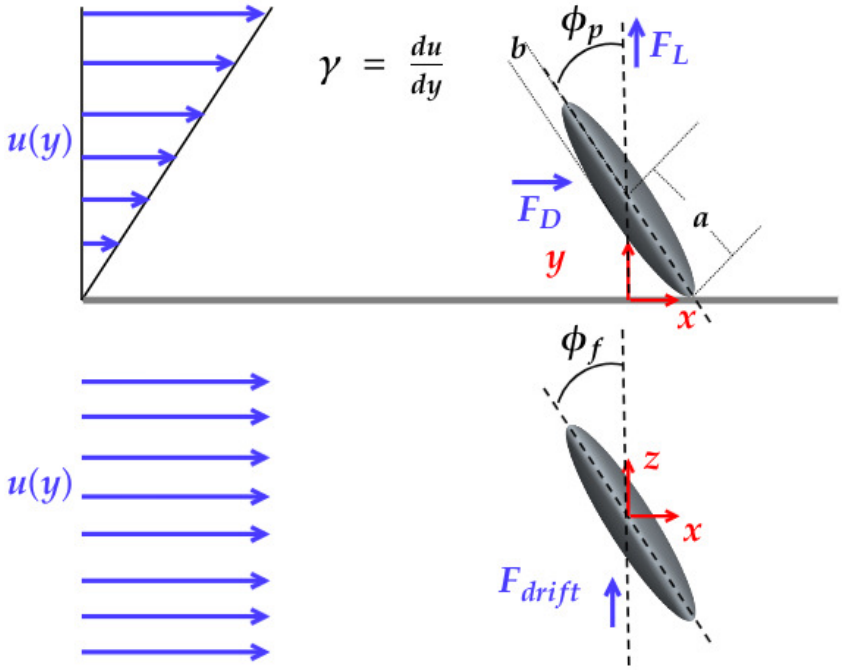

Figure 1. Schematic diagram of an oblate spheroid-on-a-smooth-surface in linear shear flow. Top: a side-view (xy-plane) with the velocity profile $u(y)$; Bottom: top-view (xz-plane)with the velocity profile $u(y)$.

where, $U_c = a\gamma$ is the undisturbed fluid velocity at the mass center of the oblate spheroid, $y = a$, and ν the kinematic viscosity of the fluid. All spheroids in this work have the same volume equivalent spherical diameter $d_p = 2\mathrm{a}\lambda^{1/3}$.

A. Dimensionless particle dynamic coefficients

Depending on the particle position, shape and orientation, the interaction between the fluid flow and the spheroid results in different hydrodynamic forces experienced by the spheroid. In addition to the body force of gravity and the adhesion force, an isolated oblate spheroid attached to a smooth plane in a fluid flow experiences drag and lift forces. These hydrodynamic forces are characterized by the dimensionless coefficients, C_D and C_L respectively, and are defined as a function of the diameter of the volume equivalent sphere, d_p:

$$C_D = \frac{8\|\mathbf{F}_D\|}{\rho_f \pi d_p^2 U_c^2}, \tag{2}$$

$$C_L = \frac{8\|\mathbf{F}_L\|}{\rho_f \pi d_p^2 U_c^2}, \tag{3}$$

Here, $\mathbf{F}_D$ and $\mathbf{F}_L$, are, respectively, the drag and lift forces experienced by the oblate spheroid-on-a-smooth-surface immersed in a fluid with density ρ_f.

Moreover, in the case of spheroids (prolate or oblate), when the axis of symmetry is neither aligned nor perpendicular to the flow direction ($\phi_f \neq 0^o$ and $\phi_f \neq 90^o$), an asymmetry of flow structure about the drag-lift plane ($xy - plane$) induces a lateral force in the z-direction. This force is so-called "drift" force, as shown in Naghashnejad et al.[50], $\mathbf{F}_{drift}$. On the other hand, due to the symmetry of such particle shape with respect to the drag-lift plane ($xy-plane$), the drift force vanishes for the sphere and the spheroids with an axis of symmetry aligned or perpendicular to the flow direction.

To characterize the drift force, we defined here the drift coefficient C_{drift} as :

$$C_{drift} = \frac{8\|\mathbf{F}_{drift}\|}{\rho_f \pi d_p^2 U_c^2}. \tag{4}$$

Dealing with flow over a single sphere-on-a-smooth-surface and by fitting the computational results of the drag and lift coefficient, Zeng et al.[39] have obtained the following correlation for the drag coefficient:

$$C_D = 1.7009\frac{24}{Re_p}\left[1 + 0.104 Re_p^{0.75}\right], \tag{5}$$

and for the lift coefficient by:

$$C_L = \frac{3.663}{\left(Re_p^2 + 0.1173\right)^{0.22}} \tag{6}$$

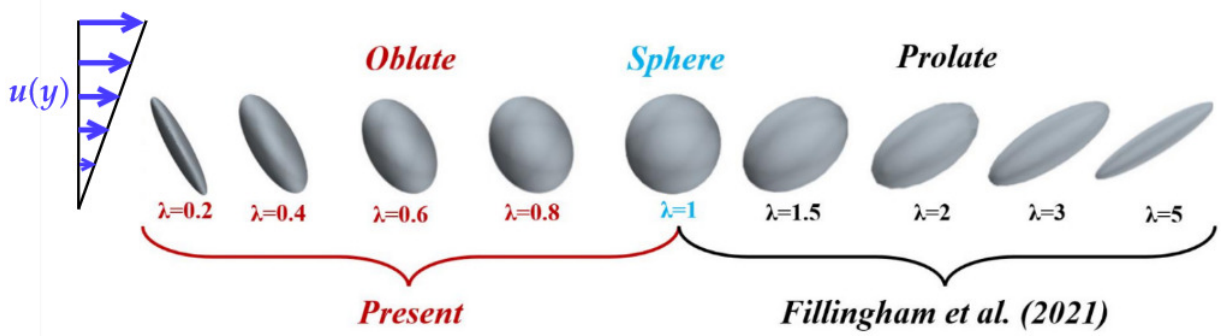

Figure 2. Illustration of the particles considered in the present study. Particles studied by Fillingham et al.[47] are also reported to motivate the reader.

As revealed in the literature review, there is a lack of correlations for these hydrodynamic coefficients acting on non-spherical particles, especially spheroids. Therefore, the present work is devoted to providing those coefficients for the oblate spheroid-on-smooth-surface.

The following sections outline the computational methodology used in the present work, including the validation of the computed hydrodynamic coefficients.

III. COMPUTATIONAL METHODOLOGY

In order to achieve the objective defined for this study, the relevant physical parameters governing our investigation, namely, particle aspect ratio, particle orientation, and particle Reynolds number, have to be selected. In addition, the domain size, the number of mesh nodes, the Navier-Stokes solver, and the computation of the hydrodynamic forces have to be assessed. Thus, this section is devoted to exposing and validating the computational methodology.

A. Particle parameters

In the context of this study, which deals with oblate spheroids-on-a-smooth-surface, four parameters are considered for acquiring a helpful database for developing the models predicting these hydrodynamic coefficients. The range values of the dimensionless parameters considered in the computational fluid dynamics conducted in this study are summarized in Table I. Figure 2 was sketched to illustrate the different types of spheroids considered in this study. To contextualize our survey and to motivate the reader, the prolate spheroids studied by Fillingham et al.[47] are also depicted in the same figure. It is essential to highlight that we have only varied the flow orientation, ϕ_f, and the pitch angle was kept constant, $\phi_p = 0^o$, in order to be in accordance with the investigation by Fillingham et al.[47]. Furthermore, in some applications, the maximum particle Reynolds number of small particles located within the viscous sub-layer of a turbulent flow where a local linear shear flow exists is overall of the order of 10[47,50,55]. Therefore, consistent with this statement and to also keep a similar range of particle Reynolds number as in Fillingham et al.[47], our simulations were performed for Re_p up to 7.

Table I. Range values of the dimensionless parameters of the simulations

Dimensionless Parameters	Range
Aspect ratio λ	0.2, 0.4, 0.6, 0.8 and 1
Flow orientation angle ϕ_f	0^o, 30^o, 45^o, 60^o and 90^o
Particle pitch angle ϕ_p	0^o
Particle Reynolds number Re_p	0.1, 0.2, 0.5, 1, 2, 3, 5 and 7

B. Governing equations

In the present study, we consider a laminar, incompressible and isothermal flow of a Newtonian fluid over a single oblate spheroids-on-a-smooth-surface. In addition, Zarghami & Padding[56] showed that the flow remains steady for a single 2D elliptical particle for $Re_p \leq 50$. Furthermore, as stated by Zeng et al.[39] for the sphere, Fillingham et al.[47] for the prolate spheroid and Naghashnejad et al.[50] for the hemispheroid, the flow field around such particle remains steady for a particle Reynolds number up to 10. Accordingly, it was deemed appropriate to consider the flow steady, and the time-dependent term in the Navier–Stokes equations has been neglected. The final form of governing equations reads as:

$$\nabla \cdot \mathbf{u} = 0, \tag{7}$$

$$(\mathbf{u} \cdot \nabla)\mathbf{u} = -\frac{1}{\rho_f}\nabla p + \nu \Delta \mathbf{u}, \tag{8}$$

where p is the pressure.
The hydrodynamic forces are the components of the fluid

forces acting on the considered particle in the three principal directions. These forces are obtained by integrating the total stress acting on the particle surface area:

$$\mathbf{F} = \oint_S \left[-p\mathbf{n} + \mu(\nabla\mathbf{u} + \nabla\mathbf{u}^{\mathbf{T}}) \cdot \mathbf{n}\right] \mathrm{d}S. \tag{9}$$

Here, the drag force $F_D = \mathbf{n_x} \cdot \mathbf{F}$ is the force acting in the x direction, $F_L = \mathbf{n_y} \cdot \mathbf{F}$ is the force acting in the y direction, and $F_{drift} = \mathbf{n_z} \cdot \mathbf{F}$ is the force acting in the z direction.

Simulations are performed using the Computational Fluid Dynamics (CFD) commercial software STARCCM+© version 17.02.07. The centered scheme is used for discretizing all the numerical fluxes in the Navier–Stokes equations. The problem of the coupling between velocity and pressure is tackled with a Semi-Implicit Method for Pressure-Linked Equations (SIMPLE)[57].

C. Computational domain and boundary conditions

Oblate spheroids with four different aspect ratios, with angles of inclination ϕ_f and ϕ_p were considered (see Table I). Each spheroid was placed in the domain shown in Figure 3. Because of the asymmetry of the problem, a complete 3D configuration is considered in all simulations. The geometrical configuration is a parallelepiped fluid box surrounding the spheroid. The simulation domain where the $length \times width \times height$ of $36d_p \times 12d_p \times 12d_p$ was previously reported adequate and used by Derksen & Larsen[58] and Ting et al.[48]. In the simulations performed by Fillingham et al.[47], the domain size of $D_{50d_p \times 10d_p \times 10d_p}$ which were reported to be adequate to capture the physical behaviour of the flow over a sphere-on-a-surface. This domain size is tested in comparison to two larger domains, in order to prevent any disturbance of the flow due to the lateral boundary conditions. The three domain sizes tested are: $(D_1 : 50d_p \times 10d_p \times 10d_p)$, $(D_2 : 50d_p \times 10d_p \times 15d_p)$ and $(D_3 : 50d_p \times 10d_p \times 20d_p)$. Simulations have been performed for the case of oblate spheroid with an aspect ratio of $\lambda = 0.2$ at $Re_p = 0.1$ and $Re_p = 7$ for $\phi_f = 45^o$ (Tab.II and Tab.III).

Table II. Influence of varying domain size on the drag, lift and drift coefficient for an oblate for $\phi_f = 45$ and $Re_p = 0.1$.

Domain	C_D	Δ_{C_D}	C_L	Δ_{C_L}	C_{drift}	$\Delta_{C_{drift}}$
D_1	497.949		5.946		-102.9	
D_2	493.206	0.962	5.8	2.519	-101.377	1.481
D_3	491.341	1.345	5.804	2.452	-100.884	1.96

The deviations in the drag, lift, and drift coefficients obtained with the smallest domain size D_1 compared to the results for the larger domains D_2 and D_3 are found to be less than 4% for both $Re_p = 0.1$ and $Re_p = 7$.

Table III. Influence of varying domain size on the drag, lift and drift coefficient for $\phi_f = 45^\circ$ and $Re_p = 7$.

Domain	C_D	Δ_{C_D}	C_L	Δ_{C_L}	C_{drift}	$\Delta_{C_{drift}}$
D_1	24.078		2.719		-10.624	
D_2	23.593	2.014	2.652	2.464	-10.321	2.852
D_3	23.417	2.745	2.630	3.273	-10.216	3.840

Accordingly, it can be reasonably concluded for the domain D_1 that the perturbation of the flow due to lateral boundary conditions does not have a significant adverse effect on the computational results. Therefore, the computational domain chosen in the present work is $D_1 : 50d_p \times 10d_p \times 10d_p$. It is worth mentioning that, similar to Fillingham et al.[47], each spheroid was modeled with a small gap away from the surface corresponding to $0.01d_p$ to avoid singularity at the contact point between the spheroid and the surface, which is a challenge to mesh generation. A linear velocity profile is imposed in the inlet boundary $u(x = 0) = \gamma y$, the upper wall is moving at a steady velocity of $u(L_y) = \gamma L_y$. A pressure outlet condition is chosen, and the no-slip Dirichlet condition is applied at the particle surface and on the bottom channel wall, while the sidewalls are specified as symmetry boundaries.

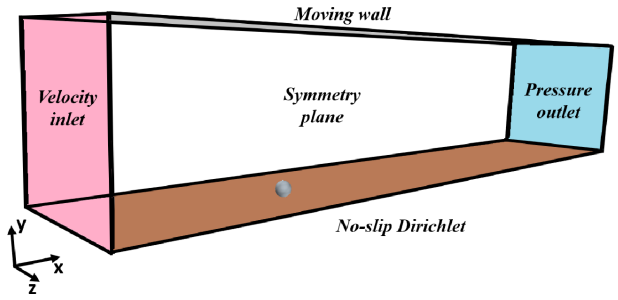

Figure 3. Schematic description of the computational domain showing the particle position and indicates the boundary conditions.

D. Grid independence

The body-fitted approach was used to mesh the fluid domain. The mesh of the fluid domain consists of unstructured polyhedral control volumes. In addition, the surface mesh of the spheroid is kept fine enough to ensure a precise integration of the hydrodynamic forces acting on the surface. To reduce the overall computational cost, a hybrid mesh is created for the domain. In particular, the computational mesh grid is clustered in areas close to the particle and behind the particle to capture a possible wake. The mesh generated for the case of a sphere-on-a-surface is shown in Figure 4.

Numerical simulation by CFD requires, at the first step, to conduct a grid-independence study. For this pur-

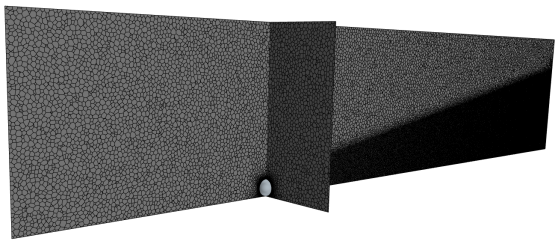

Figure 4. Computational mesh domain showing the refinement around a sphere-on-a-smooth-surface and behind the sphere used in this research.

pose, the influence of the mesh resolution is tested with the flow around an isolated sphere-on-a-smooth-surface, for three different meshes (coarse, medium, and fine). This test is conducted at the particle Reynolds number, $Re_p = 7$, and the results are summarized in Table IV. These relative deviations are calculated using the given formulas:

$$\Delta_{C_D} = \left| \frac{C_D - C_{D,Ref}}{C_{D,Ref}} \right| \times 100\%, \tag{10}$$

and

$$\Delta_{C_L} = \left| \frac{C_L - C_{L,Ref}}{C_{L,Ref}} \right| \times 100\% \tag{11}$$

Here $C_{D,Ref}$ and $C_{L,Ref}$ correspond respectively to the results obtained with the finest grid.

Table IV. Influence of varying CFD basecase mesh resolution on the drag and lift coefficient for a sphere-on-surface and $Re_p = 7$.

		Drag coefficient		Lift coefficient	
Resolution	Number	CFD	Δ_{C_D}	CFD	Δ_{C_L}
Fine	14362588	8.564		1.582	
Medium	8107542	8.560	0.05	1.580	0.126
Coarse	4458925	8.452	1.31	1.547	2.21

Even though, the coarse mesh provides a correct result, the medium mesh was used. However, it is not necessary to refine beyond the medium mesh. Indeed, from a quantitative point of view, the differences between the results obtained from the medium grid and the finest grid, are of 0.05% for the drag coefficient and of 0.126% for the lift coefficient. On the other hand, the differences between the results computed by the coarse grid and the finest grid are respectively of 1.31% and 2.21%, for the drag and lift coefficients. These differences indicate that the solution is grid independent with medium and fine mesh resolution. Therefore, the best compromise between accuracy and simulation duration in all cases is meshing with a number of cells greater than 8 million cells, considering wake refinement.

E. Validation of the simulations

A comparison of the present computational results with the literature is of practical interest since it allows to validate the actual numerical approach for the computation of the hydrodynamic forces.

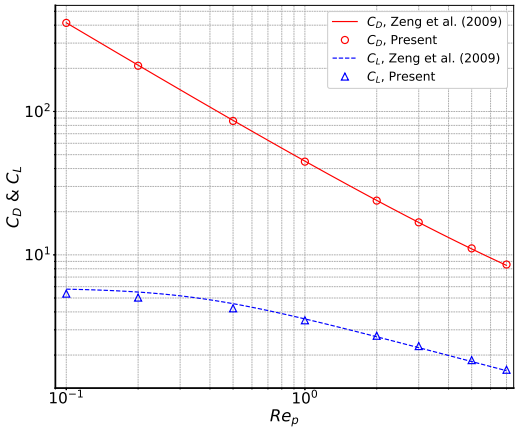

Figure 5. Validation of the computational approach showing a comparison between the computed drag and lift coefficients for a sphere-on-smooth-surface and the correlations given by Zeng et al. Eqs.(5-6).

For this purpose, our computational results in the case of the flow over a single sphere-on-a-smooth-surface were compared to the corresponding values obtained from the correlations of Zeng et al.[39] (Eqs.5-6). As presented in Figure 5, it can be observed that our computational results collapse reasonably well with the correlations from Zeng et al.[39], for both drag and lift coefficients and whatever the particle Reynolds number.

To quantify the differences, the computed values of C_D and C_L and the corresponding values from equations (5-6) are given in Table V, along with the relative deviations between the computational results and the results from equations (10-11), for each particle Reynolds number considered in this study. The relative deviation never exceeds 1.5% for C_D whereas the relative deviation of the computed C_L attains 8.5% at small Re_p. Furthermore, a comparison can be made with the values extracted from the Direct numerical simulation of Zeng et al.[39]. The extracted values at $Re_p = 2$ are $C_D = 24.188$ and $C_L = 2.702$ from which our results deviate respectively by 1.21% and 0.96%. Clearly, there is a good agreement between the computed results and both the computed and the correlations established by Zeng et al.[39].

Validation case of the simulations in the case of prolate spheroids was conducted by comparing the results with the correlations provided by Filligham et al.[47]. Especially, comparisons were made for the drag and lift coefficients for two aspect ratios, $\lambda = 1.5$ and $\lambda = 2$, at the incidence angles $\phi_f = 0°$ and $\phi_f = 90°$. The graphical comparison, shown in Figure 6, and the mean and maximum relative deviations, computed in Tables (VI-VII),

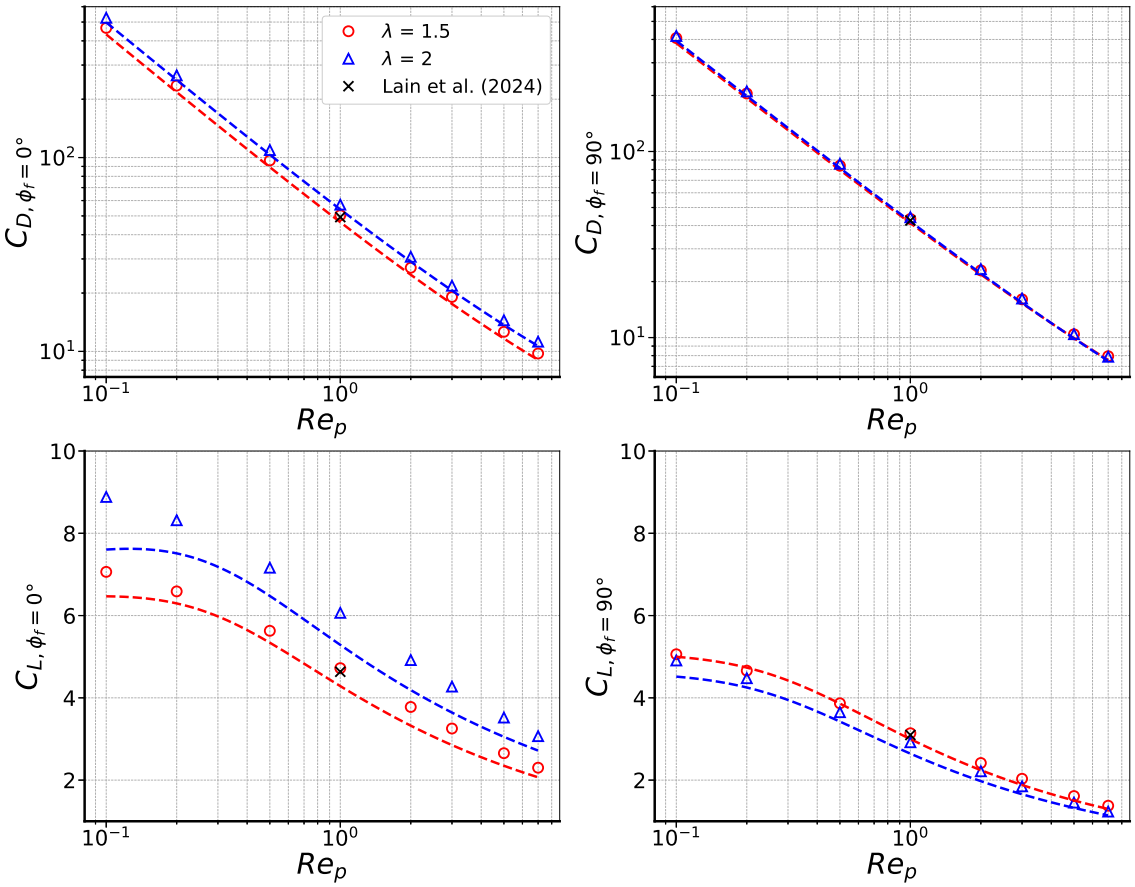

Figure 6. Validation of the computational approach showing a comparison between the computed results (symbols) and the correlations provided by Filligham et al.[47] (Dashed lines), for drag and lift coefficients in the case of prolate spheroid-on-smooth-surface.

Table V. Drag and lift coefficients for a sphere-on-a-surface.

	Drag coefficient C_D			Lift coefficient C_L		
Re_p	CFD	Eq.5	Δ_{C_D}	CFD	Eq.6	Δ_{C_L}
0.1	414.88	415.77	0.21	5.360	5.765	6.93
0.2	208.45	210.46	0.96	5.035	5.502	8.50
0.5	85.90	86.69	0.92	4.237	4.566	7.20
1	44.69	45.07	0.84	3.496	3.575	2.21
2	23.90	23.98	0.35	2.728	2.683	1.69
3	16.85	16.83	0.12	2.310	2.250	2.56
5	11.10	11.00	0.86	1.844	1.802	2.31
7	8.56	8.44	1.40	1.580	1.550	1.61

illustrate the good accordance between the computed results and the correlations provided by Fillingham et al.[47].

In Figure 6, we reported also the numerical results obtained by Lain et al.[54] at $Re_p = 1$ and $\phi_p = 0°$ at the orientation angles $\phi_f = 0°$ and $\phi_f = 90°$ and for an aspect ratio $\lambda = 1.5$. The extracted values at $\phi_f = 0°$ are $C_D = 49.3$ and $C_L = 4.63$ from which our results deviate respectively by 2.17% and 1.85%, and for $\phi_f = 90°$ are $C_D = 42.57$ and $C_L = 3.1$ from which our results deviate respectively by 1.91% and 1.353%. Our results are clearly in good agreement with the results reported by Lain et al.[54]. Moreover, we have performed simulation for an oblate spheroid with ($Re_p = 0.1$, $\lambda = 0.5$, and $\phi_f = 0^o$). To make a comparison with the analytical solution for a spheroid in the Couette flow, given by Wakiya[34], the position of the spheroid center is located at a distance from the surface of $2a$. The obtained computational result $C_D = 458.42$ is confronted to the deduced result from the analytical solution provided by Wakiya[34] $C_D = 475.96$. The deviation is found to be of 3.83%, indicating an accurate estimation of the drag coefficient.

Table VI. Mean relative deviations of the CFD results from the correlations by Fillingham et al.[47].

	$\overline{\Delta_{C_D}}$		$\overline{\Delta_{C_L}}$	
	$\phi_f = 0^o$	$\phi_f = 90^o$	$\phi_f = 0^o$	$\phi_f = 90^o$
$\lambda = 1.5$	8.36	5.42	10.18	4.58
$\lambda = 2$	5.68	5.50	14.49	9.10

Given the discussion above, it is fair to summarize here that this validation case, in combination with the distinct computational details, the current numerical approach is satisfactorily validated. Accordingly, this computational

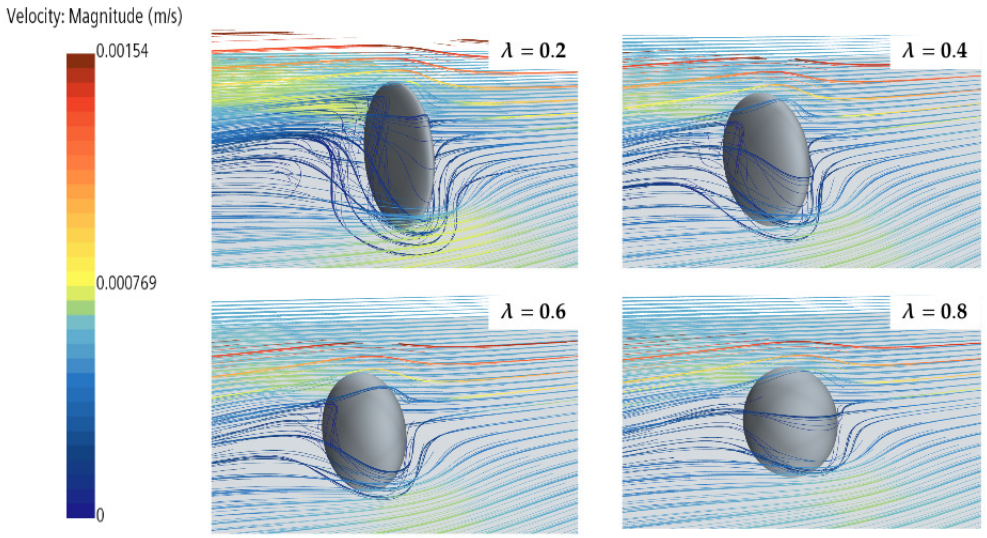

Figure 7. Illustration of the shear flow around the four oblate spheroid-on-surface considered for $Re_p = 7$ and $\phi_f = 0^o$. In this illustration, the flow comes from right to left.

Table VII. Maximum relative deviations of the CFD results from the correlations by Fillingham et al.[47].

	$\max \Delta_{C_D}$		$\max \Delta_{C_L}$	
	$\phi_f = 0^o$	$\phi_f = 90^o$	$\phi_f = 0^o$	$\phi_f = 90^o$
$\lambda = 1.5$	8.692	6.500	14.128	8.016
$\lambda = 2$	5.900	6.143	17.416	12.168

methodology is employed in all simulations of the flow over an isolated spheroid-on-a-surface considered in the present investigation, from which hydrodynamic forces are determined.

IV. RESULTS AND DISCUSSIONS

The motivation for this investigation is the need for correlations for the hydrodynamic coefficients in the context of oblate spheroid-on-a-surface, which are encountered in many environmental and industrial processes as discussed above. Having presented herein before a convincing validation of the numerical approach, in this section, the flow visualization and the computed hydrodynamic coefficients are presented along with the methodology used to develop the new correlations. Additionally, we address some comments on the performance of the derived predictive correlations.

A. Flow visualization

A first qualitative analysis can be done by examining briefly the flow past the spheroids in the present configuration, which is of particular interest. It is obvious that the flow structure around the particle varies depending on the particle's orientation relative to the flow direction. In figure 7, we display the streamlines for the four spheroids with the symmetry axis aligned with the flow $\phi_f = 0^o$ at particle Reynolds number $Re_p = 7$. Consistent with the presence of the surface, it can be seen that the wake structure formed behind the spheroid is three-dimensional, whatever the aspect ratio. Thus, it was essential to have considered a complete 3D configuration for our simulations.

It can be particularly seen that the flow became more complex in the wake of the spheroid as the aspect ratio decreased. This behaviour is consistent with observations by Lain et al.[54] who noticed a complex structure and massive stall flow behind the oblate ellipsoid of aspect ratio $\lambda = 0.2$. As stated in Ouchene[26], intuitively, in view of the fact that the frontal area is circular for all spheroids $\phi_f = 0^o$ at this orientation, only the shape (curvature) can explain this behavior. Moreover, based on the complex structure of the wake flow noticed at this particle Reynolds number, one may expect and anticipate an unsteadiness of the flow at a particle Reynolds number slightly higher than 7 in the case of a oblate spheroid with an aspect ratio of 0.2.

B. Drag coefficient

The behavior of the drag coefficient for oblate spheroids-on-a-surface as a function of the particle Reynolds number is reported in Figure 8 for the different aspect ratios considered in the present work. We first selected and depicted the computational results at the extremum orientation angles, $\phi_f = 0^o$ and $\phi_f = 90^o$,

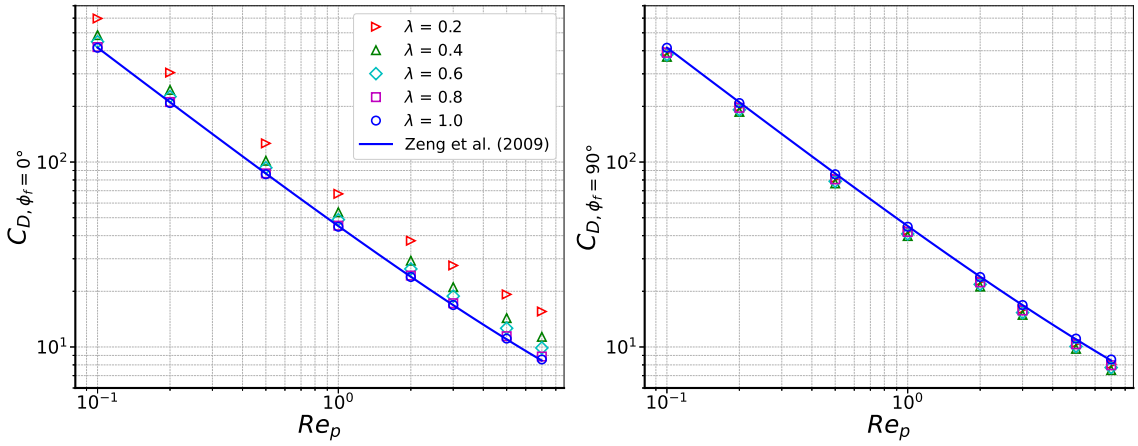

Figure 8. Drag coefficient from the present CFD against particle Reynolds number for the orientation angles $\phi_f = 0^o$ and $\phi_f = 90^o$ at all aspect ratios.

along with the equation (5) for comparison. Similar to a sphere, it can be seen that, for both extremum angles, C_D decreases as Re_p increases, whatever the aspect ratio. In addition, the drag coefficient departs significantly from equation (5) when the axis of symmetry is aligned with the flow direction $C_{D,\phi_f=0^o}$ compared to the case of the symmetry axis perpendicular to the flow direction $C_{D,\phi_f=90^o}$, for which only a slight departure from the spherical case is noticed. Furthermore, the simulation predicts a monotonic increase in the drag coefficient $C_{D,\phi_f=0^\circ}$ as the aspect ratio decreases (Figure 14). However, when the shape deviates from that of a sphere, a non-monotonic behavior in the drag coefficient $C_{D,\phi_f=90^\circ}$, is observed, irrespective of the particle Reynolds number. These observations are in accordance with the earlier results reported by O'donnell and Helenbrook[59] and Ouchene[26] in the case of a spheroid in a uniform flow. Moreover, the dependence of the drag coefficient on the aspect ratio is seen to be more pronounced at higher Re_p. Expectedly, the effect of the aspect ratio on the drag coefficient differs from the observation by Fillingham et al.[47] in the case of prolate spheroids. Indeed, as the elongation increases, the frontal area $A_\perp$ at $\phi_f = 90^\circ$ grows larger and increasingly exceeds the circular frontal area $A_\parallel$. Conversely, at $\phi_f = 0^\circ$, the frontal area $A_\perp$ decreases for oblate spheroids, gradually becoming smaller than the circular frontal area $A_\parallel$.Intuitively, one can argue that such geometrical differences would be behind the way the trend of C_D departs from the spherical case.

Following the methodology employed by Ouchene et al.[24,26] to derive a correlation for C_D for spheroid with a link to the spherical case, it is obvious that the predicting model has to reduce to the correlation given by Zeng et al.(Eq. 5). A similar approach was helpfully used by Fillingham et al.[47] in the case of prolate spheroids.

Based on the observed variations of the drag coefficient with respect to particle Reynolds number, aspect ratio, and incidence angle, the general form of the correlation can be derived from previous studies as follows:

- The drag coefficients for $\phi = 0^\circ$ and $\phi = 90^\circ$ vary according to the particle Reynolds number.
- The aspect ratio λ is considered the primary shape parameter for the spheroids.
- The correlation must reduce to the Zeng et al. correlation (Eq. 5) when $\lambda = 1$, corresponding to a sphere.

Therefore, the functional form of the derived correlation for $C_{D,\phi_f=0^o}$ and $C_{D,\phi_f=90^o}$ is given by :

$$C_D = 1.7009\frac{24}{Re_p}\left[\lambda^{d_1} + 0.104\lambda^{d_2}Re_p^{0.75} + d_3(1-\lambda)^{d_4}Re_p^{d_5}\right] \tag{12}$$

The best fitting of the computational results based on this functional form gives the fit parameters summarized in Table VIII. They are provided for both parallel and perpendicular alignment of the symmetry axis with the flow direction. The accurate estimation of the drag coefficient is given in the range of $Re_p \in [0.1 - 7]$ for $\lambda \in [0.2 - 1]$. These correlations predict the drag coefficient with the mean relative deviations of $\overline{\Delta_{C_{D,\phi_f=0^o}}} = 1.11\%$, and $\overline{\Delta_{C_{D,\phi_f=90^o}}} = 1.26\%$, and the maximum relative deviations of $\max(\Delta_{C_{D,\phi_f=0^o}}) = 3.86\%$ and $\max(\Delta_{C_{D,\phi_f=90^o}}) = 5.45\%$. Here, the relative deviation is calculated using equation (10) where, $C_{D,Ref} = C_{D,CFD}$ and C_D correspond to the results obtained by the equation (12) at the corresponding orientation angle ϕ_f.

At this stage, the correlations for $C_{D,\phi_f=0^o}$ and $C_{D,\phi_f=90^o}$ have been drawn, but the correlation accounting for the particle orientation remains to be determined. In the case of uniform flow over spheroids in the Stokes regime flow, the drag coefficient is provided by Happel &

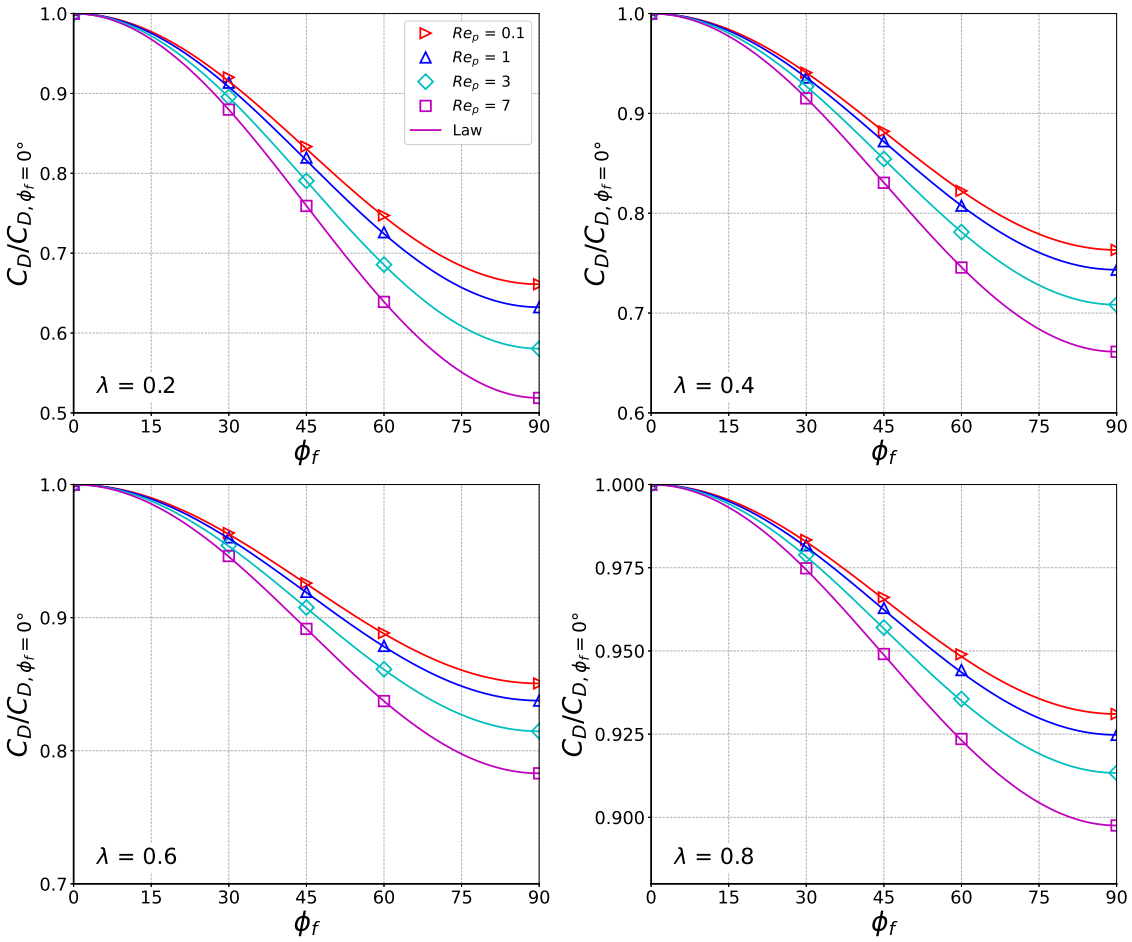

Figure 9. Normalized drag coefficient from the present CFD as a function of the orientation angle ϕ_f for Re_p = 0.1, 1, 5 and 7. Equation (14) is depicted for comparison.

Table VIII. Fitting parameters for the correlation of the drag coefficient at $\phi_f = 0^o$ and $\phi_f = 90^o$ (Eq.12).

	d_1	d_2	d_3	d_4	d_5
$\phi_f = 0^o$	-0.2822	-0.6514	-0.2487	0.7853	0.1024
$\phi_f = 90^o$	0.2615	0.1201	0.6255	3.441	-0.00655

Brenner[60] is given by:

$$C_D = C_{D,\phi_f=0^o} + \left(C_{D,\phi_f=90^o} - C_{D,\phi_f=0^o}\right)\sin^2(\phi_f) \tag{13}$$

This formula is examined in different numerical investigations. Ouchene et al.[24], Sanjeevi and Padding[61], Sanjeevi et al.[25] and Ouchene[26] observed that this relationship performs well outside the Stokes regime flow. Fillingham et al.[47] retrieved a similar trend for prolate ellipsoid-resting-on-a-surface. Recently, Lain et al.[54] noticed the same trend by varying the pitch angle, in the configuration of linear shear flow over spheroids. At a low particle Reynolds number, Chéron & van Wachem[52] noticed in the case of rod-like particles that the profile of the scaled drag coefficient as a function of the orientation angle closely resembles that of the drag coefficient obtained in a uniform flow. However, at higher particle Reynolds numbers, $Re_p > 10$, the evolution of the drag coefficient as a function of the orientation angle scaled by the drag coefficient in the case of uniform flow no longer maintains its symmetry at the pitch angle $\phi_p = 90^o$. Accordingly, instead of performing a fitting of the computational results, the relevant functional form of the drag coefficient as a function of the orientation angle is the equation (13), which is tested in comparison with the computational results. For the sake of clarity, orientation dependence of the drag coefficient is analyzed from the normalized drag coefficient, which is defined as a ratio between the drag coefficient at the considered angle and the drag coefficient at the angle, $\phi_f = 0^o$:

$$\frac{C_D}{C_{D,\phi_f=0^o}} = 1 + \left(\frac{C_{D,\phi_f=90^o}}{C_{D,\phi_f=0^o}} - 1\right)\sin^2(\phi_f) \tag{14}$$

Figure 9 shows a graphical comparison of the computational results with the theoretical normalized drag from Happel & Brenner[60] over the range of λ. The solid lines

represent the (Eq. 14). As it can be seen, the influence of the orientation angle is substantial and increases with an increase in the particle Reynolds number. In addition, diminishing the value of the aspect ratio contributes to the increase in the influence of particle orientation. Furthermore, the square sine law reported in equation (14) matches well with the current computational results. The mean relative deviation from computational results is of the order of 0.5%. This means that the analytical formula provided by Happel & Brenner[60] for the evolution of the drag coefficient as a function of the orientation likewise remains valid in the case of an isolated oblate spheroid-on-a-surface. Interestingly, this was also retrieved by Fillingham et al.[47] in the case of prolate ellipsoid-resting-on-a-surface in the range of $Re_p \in [0.1-10]$ and $\lambda \in [1-5]$. Therefore, one may conclude the validity of the square sine function in both prolate and oblate spheroids in at least the range of $Re_p \in [0.1-7]$ and $\lambda \in [0.2-5]$.

As a measure of the complete model accuracy, we computed the mean and the maximum relative deviations between the predicted and computed values of the drag coefficient over the entire data set, which were found to be of $\overline{\Delta_{C_D}} = 0.52\%$ and $\max(\Delta_{C_D}) = 5.45\%$, respectively. Giving these deviations, we can conclude that the derived correlation gives an excellent prediction of the the drag coefficient as a function of the particle Reynolds number, the aspect ratio and the particle orientation with respect to the flow.

C. Lift coefficient

The variations of the lift coefficient with respect to the particle Reynolds number is depicted in Figure 10 for all the considered aspect ratios. Similar to the drag coefficient, results are displayed at extremum orientation angles, $\phi_f = 0^o$ and $\phi_f = 90^o$ along with the correlation given by Zeng et al.[39] for comparison (Eq.6). As for the sphere, oblate spheroids experience a non-zero lift induced by the shear flow. It can be seen that, for both extreme angles, the lift coefficient C_L decreases as the particle Reynolds number increases, regardless of the aspect ratio. In addition, the lift coefficient departs from the spherical case and the differences are more pronounced when $\phi_f = 90^o$. Especially at this orientation, a monotonic decrease of the lift coefficient is observed when the aspect ratio is diminished. In opposite, when the axis of symmetry is aligned with the surface, the lift coefficient increases as the shape gets away from the sphere. However, as the Reynolds particle number increases, the effect of shape is reduced. Similar to the drag coefficient, correlations of the lift coefficient are established at the extremum orientation angles, $\phi_f = 0^o$ and $\phi_f = 90^o$. These correlations are linked together to achieve a general treatment that accounts for particle orientation. At the extremum orientation angles, the functional form of these correlations is inspired by the correlation of the lift coefficient provided by Zeng et al.[39] in the case of a sphere-on-a-surface. Our formulation contains the terms for incidence angle, the Reynolds particle number, and a stand-alone aspect ratio term. In addition, the correlation must be reduced to the correlation provided by Zeng et al.[39] (Eq.6) when the aspect ratio is $\lambda = 1$ corresponding a sphere. This particular choice is motivated by the fact that Zeng et al.[39] used the result by Leighton and Acrivos[37] to close their correlation predicting the lift coefficient of a spherical particle. Thus, the proposed correlation has to reduce to the equation (Eq. 6). Specifically, these correlations are given by:

$$C_L(\phi_f = 0^o \; or \; 90^o) = \frac{3.663\left[1+\ell_1(1-\lambda^{\ell_2})Re_p^{\ell_3}\right]}{\left[\lambda^{\ell_4}Re_p^2 + 0.1173\lambda^{\ell_5}\right]^{0.22}} \quad (15)$$

By making use of the same methodology employed for the drag coefficient, a best fitting of this functional form to the computational results is performed to obtain the fit parameters listed in Table IX. The differences between the derived correlation and the computational results are evaluated through the mean and maximum relative deviations from the current computational results (eq.15. Here, $C_{L,Ref} = C_{L,CFD}$ and C_L correspond to the results obtained by the equation (15) at the corresponding orientation angle ϕ_f.

The maximum deviations are found to be $\max(\Delta_{C_{L,\phi_f=0^o}}) = 7.69\%$ and $\max(\Delta_{C_{L,\phi_f=90^o}}) = 6.7\%$, and the mean deviations, $\overline{\Delta_{C_{L,\phi_f=0^o}}} = 2.85\%$ and $\overline{\Delta_{C_{L,\phi_f=90^o}}} = 2.99\%$, indicating that the predicted correlation is reliable and accurate for the estimation of $C_{L,\phi_f=0^o}$ and $C_{L,\phi_f=90^o}$.

We now turn our attention to the effect of the spheroid orientation on the lift coefficient. To draw the correlation of C_L accounting for the spheroid orientation, we first paid specific attention to the results by Fillingham et al.[47]. The correlations established by the authors are first based on the fitting of their computational results $C_{L,\phi_f=0^o}$ and $\left(C_{L,\phi_f=90^o} - C_{L,\phi_f=0^o}\right)$ instead of fitting $C_{L,\phi_f=0^o}$ and $C_{L,\phi_f=90^o}$. According to Sanjeevi and Padding[61], the pressure distribution contributing to the drag shows a dependence on the surface normal orientation with the incoming flow in a consistent pattern, leading to a squared sine profile. It is well known that the shear-induced lift is mainly dependent on the pressure distribution, which in turn exhibits a high dependence on the orientation of the frontal area with respect to the incoming flow. Accordingly, similar to the drag coefficient, these correlations can be linked together using the square sine law. By making use of this observation, we have adopted a similar function as for the drag coefficient. Therefore, instead of trying to make any further empirical fitting for achieving a general solution, the relevant functional form of the lift coefficient as a function of the spheroid orientation to be tested reads as:

$$C_L = C_{L,\phi_f=0^o} + \left(C_{L,\phi_f=90^o} - C_{L,\phi_f=0^o}\right)\sin^2(\phi_f) \quad (16)$$

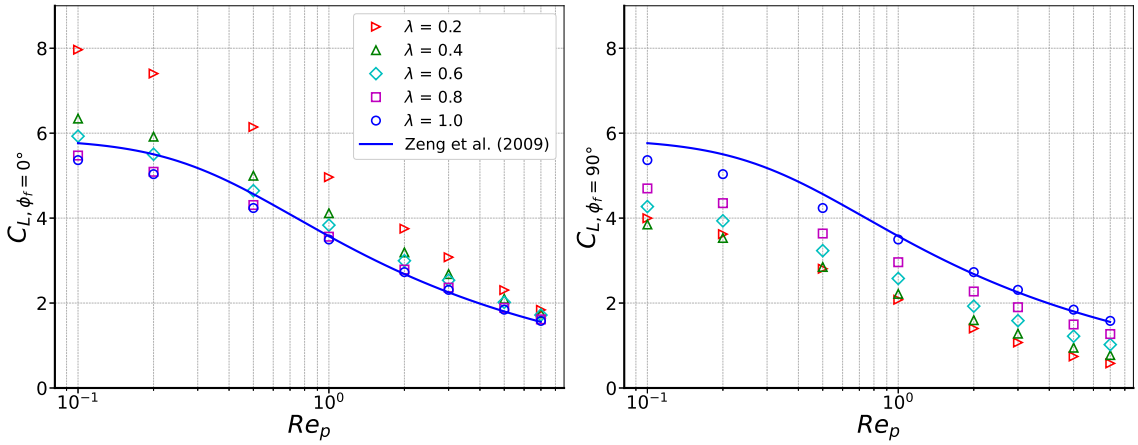

Figure 10. Lift coefficient from the present CFD against particle Reynolds number for $\phi_f = 0^o$ and 90^o, for all aspect ratios.

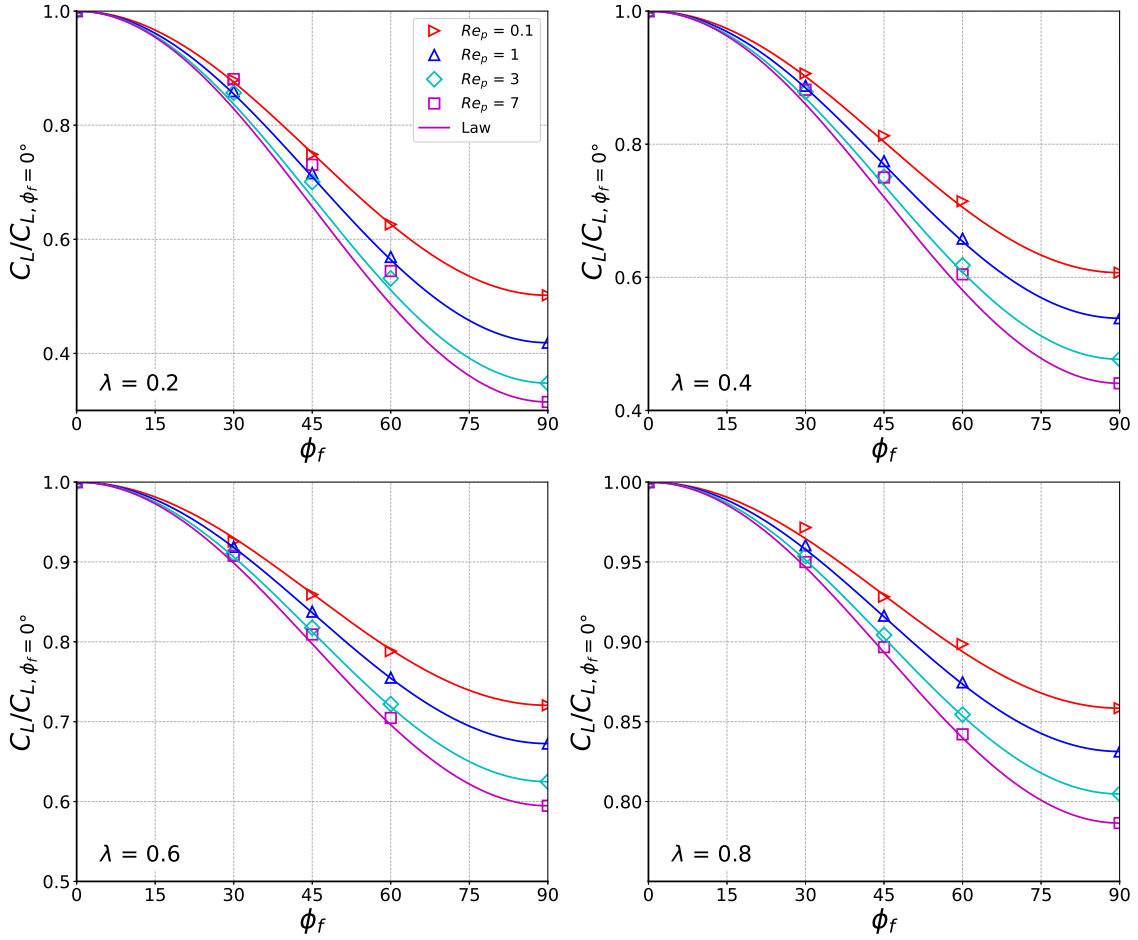

Figure 11. Normalized lift coefficient from the present CFD as a function of the orientation angle ϕ_f, for different particle Reynolds numbers. Equation (17) is plotted for comparison.

As already performed for the drag coefficient, the orientation dependence of the lift coefficient is analyzed from the normalized lift coefficient which is defined as the ratio between the lift coefficient at the considered orientation angle and the lift coefficient at the orientation angle of $\phi_f = 0^o$:

$$\frac{C_L}{C_{L,\phi_f=0^o}} = 1 + \left(\frac{C_{L,\phi_f=90^o}}{C_{L,\phi_f=0^o}} - 1\right)\sin^2(\phi_f) \qquad (17)$$

Figure 11 shows a graphical comparison of the computational results of the normalized lift coefficient with the normalized lift coefficient. The solid lines represent the predictions (Eq. 17). It can be observed that the effect of spheroid orientation on the normalized lift increases with the increasing particle Reynolds number, while diminishing the value of the aspect ratio gives rise to the increased influence of the particle orientation. Interestingly, the square sine function matches very well with the computational results. Nonetheless, it is clearly that decreasing the aspect ratio combined with the increasing of the particle Reynolds number results in an increasing deviation from the sine-squared lift law. The deviation of the computational results against the sine-squared curve is particularly more pronounced at $\lambda = 0.2$ and $Re_p = 7$. A possible explanation for this particular behavior is that the wake behind the spheroid has a higher lift contribution at intermediate angles. The effect of shear flow and particle Reynolds number combined with the orientation angle plays a key role in the location of the appearance of the recirculating zones and subsequently influences the shear-induced lift at the intermediate angles.

This result sheds a new light on the issue of the orientation dependence of the lift coefficient since it discloses a square sine evolution of the lift induced by shear, which has not been reported until now in the case of oblate spheroid. This statement in combination with the results Fillingham et al.[47] allow us to conclude the lift force coefficient induced by shear evolves as "square-sine" with respect to the spheroid orientation at least the range of $Re_p \in [0.1 - 7]$ and $\lambda \in [0.2 - 5]$.

Table IX. Fitting parameters for the correlation of the lift coefficient (Eq.15).

	ℓ_1	ℓ_2	ℓ_3	ℓ_4	ℓ_5
$\phi_f = 0^o$	-0.9712	1.561	0.01567	7.594	6.427
$\phi_f = 90^o$	-0.8288	1.755	0.05219	2.947	2.245

To provide quantitative support for the accuracy of the derived correlations, we computed the mean and the maximum relative deviations between the predicted and computed values of the drag coefficient over the entire data set, which were found to be of $\overline{\Delta_{C_{L,}}} = 1.9\%$ and $\max(\Delta_{C_L}) = 11.97\%$, respectively. On the basis of the above discussion, we can safely conclude that the derived correlation satisfactorily reproduces the computational results of the lift coefficient as a function of the particle Reynolds number, the aspect ratio and the particle orientation with respect to the flow.

D. Drift coefficient

To complete this survey, we finally examine the drift force experienced by the considered spheroids. A thorough review of the literature, particularly for the drift force in the context of particle transport, shows that the drift coefficient has not received enough attention in the literature, except in the recent investigation by Naghashnejad et al.[50]. These authors reported the drift-to-drag ratio and found that this ratio increases as the orientation angle increases to about $\phi_f = 45^o$ and then decreases to become negative with further increase in the flow orientation angle. Such a behaviour is surprising at this orientation $\phi_p = 180^o$. Unfortunately, there are no sufficient details in this investigation regarding the drift coefficient allowing the interpretation of this behaviour.

In Figure 12, the variation of the drift coefficient as a function of the particle orientation is displayed at four specific particle Reynolds numbers. The computed drift coefficient is seen to decrease as the particle shape gets closer to a sphere (the aspect ratio tends toward unity). This was expected since the drift force is only induced by the asymmetry of the flow structure about the drag-lift plane as recalled above. In addition, the increase in particle Reynolds number yields a decrease in the drift coefficient, whatever the aspect ratio and the orientation angle. On the other hand, remarkably, it is observed that, regardless of the value of the aspect ratio and particle Reynolds number, the profiles consistently display peaks at an orientation angle of $\phi_f = 45^o$. Overall, these trends are similar to those obtained previously by Ouchene[26] in the case of a spheroid in uniform flow, i.e., the drift coefficient as a function of the orientation angle of the particle follows the so-called "cosine-sine" profile, suggesting that the functional form that can reproduce the effect of orientation is:

$$C_{drift} = F(\lambda, Re_p) \sin\phi_f \cos\phi_f \tag{18}$$

Once the evolution as $\sin\phi_f \cos\phi_f$ is quantitatively tested and confirmed, the function $F(\lambda, Re_p)$ has to be retrieved by fitting the computational results at the orientation angle $\phi_f = 45^o$. Accordingly, this tendency is checked by plotting in the same figure our computational results along with the function ξ, such as :

$$\xi = 2C_{drift,CFD}(\phi_f = 45^o) \sin\phi_f \cos\phi_f \tag{19}$$

On the basis of the comparison made between the computational results and the function ξ plotted in Figure 12, we are inclined to conclude that the choice of the functional form of cosine-sine allows to accurately recover the effect of the spheroid orientation on the drift coefficient.

From the above statement, we can proceed further in deriving the correlation for the drift coefficient, accounting the dependence on the particle aspect ratio and the particle Reynolds number. While the correlations for the drag and lift coefficients were obtained on the basis of the correlations given by Zeng et al.[39], no correlation has been found in the literature for the drift coefficient in the case of the aforementioned configuration.

According to these observations, the method used to derive the new formula for the drift coefficient is based on the following points:

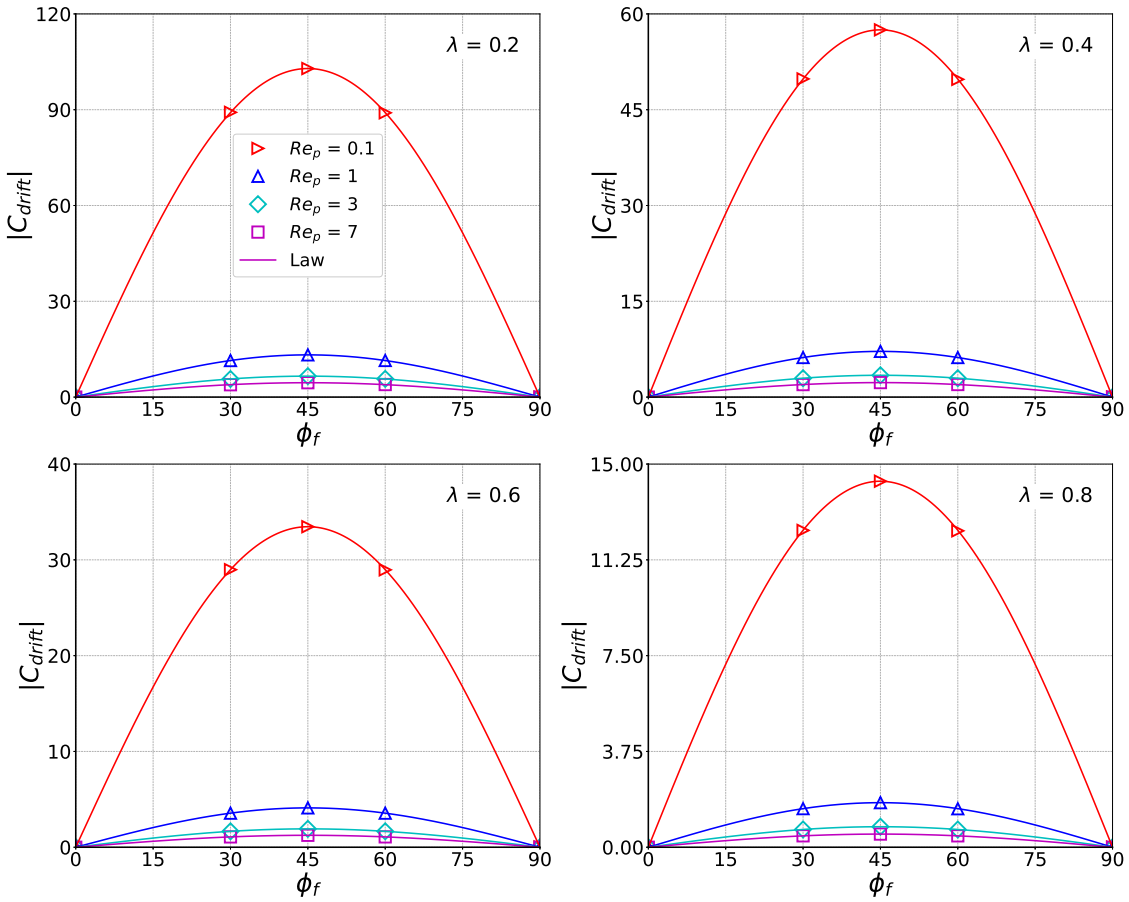

Figure 12. Drift coefficient from the present CFD as a function of the orientation angle ϕ_f, for different particle Reynolds numbers. ξ from equation (19) is also plotted for comparison.

- The drift coefficient exhibits a profile represented by the function $\sin\phi\cos\phi_f$.
- The aspect ratio λ is considered the primary shape parameter for the spheroids.
- The correlation must approach zero when $\lambda = 1$, which corresponds to a sphere that does not exhibit any drift.

Therefore, the proposed functional form of $F(\lambda, Re_p)$ respects the only criterion of the correlation that reduces to zero in the case of a sphere:

$$F(\lambda, Re_p) = \delta_1\lambda^{\delta_2}(1-\lambda^{\delta_3})Re_p^{\delta_4} + \delta_5(1-\lambda^{\delta_6})Re_p^{\delta_7} \quad (20)$$

Our formulation contains seven fitting parameters, which are listed in Table X. These parameters allow to obtain a very good agreement for the whole data set.

To evaluate the differences between the derived correlation and the computational results of the drift coefficient, we computed the mean and maximum relative deviation:

$$\Delta_{C_{drift}} = \left|\frac{C_{drift,correlation} - C_{drift,CFD}}{C_{drift,CFD}}\right| \times 100\% \quad (21)$$

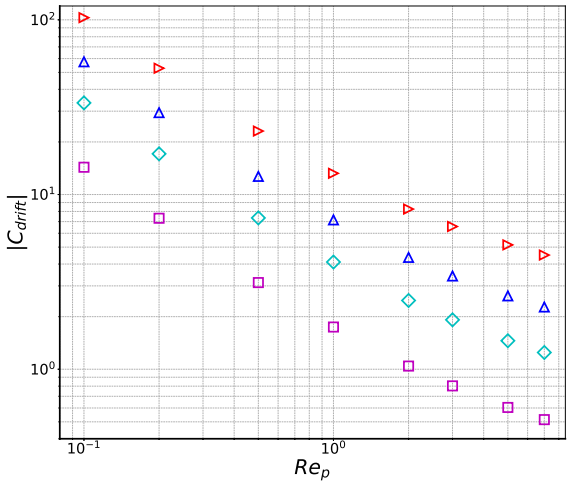

Figure 13. Drift coefficient from the present CFD as a function of Reynolds particle Re_p for $\phi_f = 45^o$.

For all aspect ratios, particle Reynolds numbers and orientation angles, the mean relative deviation is found of $\overline{\Delta_{C_{drift}}} = 2.97\%$, while the maximum relative deviation

is found to be of $\max(\Delta_{C_{drift}}) = 12.23\%$. Therefore, we can conclude that the provided correlation gives a good prediction of the drift coefficient as a function of the particle Reynolds number, the aspect ratio and the particle orientation with respect to the flow.

Table X. Fitting parameters for the correlation of the drift coefficient (Eq.20).

δ_1	δ_2	δ_3	δ_4	δ_5	δ_6	δ_7
2.2202	-0.9151	2.3500	-0.1640	123.7	0.0905	-1.0688

V. CONCLUDING REMARKS

In this work, a computation of a three-dimensional, steady Newtonian shear flow past an oblate spheroid resting on a surface was conducted. Inspired by the investigation by Fillingham et al.[47] in the case of prolate spheroids, our computational simulations were performed in a similar configuration in the case of oblate spheroids. The numerical simulations were performed varying the particle Reynolds number, $Re_p \in [0.1 - 7]$, the aspect ratio, $\lambda \in [0.2 - 1]$, and the orientation angle, $\phi_f \in [0^o - 90^o]$. The computational approach was carefully validated by testing the sensibility to the mesh variation and by comparing the computational results of the drag and lift experienced by a sphere-on-a-surface with the correlations given by Zeng et al.[39] and Fillingham et al.[47] . The focus was on the derivation of correlations for the hydrodynamic drag, lift and drift coefficients, C_D, C_L and C_{drift}, respectively. The major contributions of this investigation are summarized below.

- A large database on the hydrodynamic forces acting on spheroids in the considered configuration is reported.
- Using this database, we derived predictive correlations for the hydrodynamic coefficients, namely, drag, lift, and drift coefficients. The ability of these correlations to estimate the hydrodynamic coefficients, C_D, C_L and C_{drift} is discussed through the evaluation of the mean and maximum relative deviations and by plotting the computed versus correlated results. In particular, these correlations could estimate C_D, C_L and C_{drift} with the mean relative deviations from the computational results of 0.52%, 1.9% and 2.97%, respectively. It is worth mentioning that, to our best knowledge, the drift coefficient was not studied in the literature in the context of particle transport, except in the recent investigation by Naghashnejad et al.[50].

In addition to this database and the derived correlations, the present analysis has demonstrated the following interesting findings that should be highlighted:

- It is found that the drag coefficient as a function of the spheroid orientation follows a so-called "square sine" profile.
- Surprisingly, the lift induced by the shear as a function of the spheroid orientation also follows a so-called "square sine" profile.
- The drift coefficient as a function of the spheroid orientation follows a so-called "cosine-sine" profile.

These results have implications for improving the available models used in Euler-Lagrangian simulations of oblate spheroids, especially, when studying the detachment and/or re-suspension of such particles. However, the present correlations are obtained by a fitting process of computational database. Accordingly, the range of applicability is limited to the range of the considered parameters listed above and in the case of a steady linear shear flow.

Further work planned includes the investigation of the hydrodynamic torques experienced (pitching, yawing and rolling) by the spheroids in the three directions. Additionally, similar configurations with varying the pitch angle is to be investigated.

Investigating the dynamics of an oblate spheroid on a rough wall in a linear shear flow at a low Reynolds number presents an exciting issue for future research. Indeed, while there is substantial literature available on spherical objects on substrates, as noted in Agudo et al.[62] among others, the exploration of non-spherical shapes is still relatively limited. This highlights a valuable opportunity to expand our understanding of the behavior of such particles in different substrates."

VI. SUPPLEMENTARY MATERIAL

The data that support the findings of this investigation are reproducible and are given in the supplementary material.

VII. ACKNOWLEDGMENTS

The authors gratefully acknowlege Institut Pprime and université de Poitiers for their support and funding. Numerical simulations were performed on the VISION parallel cluster; the authors are grateful to Institut Pprime for the administration of this system.

REFERENCES

[1]Yoga Satria Putra, Anthony Beaudoin, Germain Rousseaux, Lionel Thomas, and Serge Huberson. 2d numerical contributions for the study of non-cohesive sediment transport beneath tidal bores. *Comptes Rendus. Mécanique*, 347(2):166–180, 2019.

[2]K Kachiashvili, D Gordeziani, R Lazarov, and D Melikdzhanian. Modeling and simulation of pollutants transport in rivers. *Applied mathematical modelling*, 31(7):1371–1396, 2007.

[3]Ralph A Bagnold. The transport of sand by wind. *The Geographical Journal*, 89(5):409–438, 1937.

[4]Yoshihide Tominaga and Ted Stathopoulos. Cfd simulation of near-field pollutant dispersion in the urban environment: A review of current modeling techniques. *Atmospheric environment*, 79:716–730, 2013.

[5]Dominique Mourelle and Aldo R Prieto. Pollen and spores from surface samples in the campos region of uruguay and their paleoecological implications. *Acta Botanica Brasilica*, 30:351–370, 2016.

[6]JR Agudo and Andreas Wierschem. Incipient motion of a single particle on regular substrates in laminar shear flow. *Physics of Fluids*, 24(9), 2012.

[7]Justin Davis, Kartik Tiwari, and Igor Novosselov. Soot morphology and nanostructure in complex flame flow patterns via secondary particle surface growth. *Fuel*, 245:447–457, 2019.

[8]Justin Davis, Eric Molnar, and Igor Novosselov. Nanostructure transition of young soot aggregates to mature soot aggregates in diluted diffusion flames. *Carbon*, 159:255–265, 2020.

[9]Douglas W Cooper. Particulate contamination and microelectronics manufacturing: an introduction. *Aerosol Science and Technology*, 5(3):287–299, 1986.

[10]Christophe Henry, Jean-Pierre Minier, and Sara Brambilla. Particle resuspension: challenges and perspectives for future models. *Physics Reports*, 1007:1–98, 2023.

[11]Haifeng Zhang, Goodarz Ahmadi, Fa-Gung Fan, and John B McLaughlin. Ellipsoidal particles transport and deposition in turbulent channel flows. *International Journal of Multiphase Flow*, 27(6):971–1009, 2001.

[12]Pål H Mortensen, HI Andersson, JJJ Gillissen, and BJ Boersma. Dynamics of prolate ellipsoidal particles in a turbulent channel flow. *Physics of fluids*, 20(9):093302, 2008.

[13]Cristian Marchioli, Marco Fantoni, and Alfredo Soldati. Orientation, distribution, and deposition of elongated, inertial fibers in turbulent channel flow. *Physics of fluids*, 22(3):033301, 2010.

[14]F Zhao and BGM Van Wachem. Direct numerical simulation of ellipsoidal particles in turbulent channel flow. *Acta Mechanica*, 224(10):2331–2358, 2013.

[15]Lihao Zhao, Niranjan Reddy Challabotla, Helge I Andersson, and Evan A Variano. Rotation of nonspherical particles in turbulent channel flow. *Physical review letters*, 115(24):244501, 2015.

[16]B Arcen, R Ouchene, M Khalij, and A Tanière. Prolate spheroidal particles' behavior in a vertical wall-bounded turbulent flow. *Physics of Fluids*, 29(9), 2017.

[17]Rafik Ouchene, Juan Ignacio Polanco, Ivana Vinkovic, and Serge Simoëns. Acceleration statistics of prolate spheroidal particles in turbulent channel flow. *Journal of Turbulence*, 19(10):827–848, 2018.

[18]A Michel and B Arcen. Long time statistics of prolate spheroids dynamics in a turbulent channel flow. *International Journal of Multiphase Flow*, 135:103525, 2021.

[19]Antoine Michel and Boris Arcen. Translational and angular velocities statistics of inertial prolate ellipsoids in a turbulent channel flow up to reτ= 1000. *Journal of Fluid Mechanics*, 966:A17, 2023.

[20]RP Chhabra, L Agarwal, and N Kl Sinha. Drag on non-spherical particles: an evaluation of available methods. *Powder technology*, 101(3):288–295, 1999.

[21]E Loth. Drag of non-spherical solid particles of regular and irregular shape. *Powder Technology*, 182(3):342–353, 2008.

[22]Andreas Hölzer and Martin Sommerfeld. New simple correlation formula for the drag coefficient of non-spherical particles. *Powder Technology*, 184(3):361–365, 2008.

[23]Marian Zastawny, George Mallouppas, Fan Zhao, and Berend Van Wachem. Derivation of drag and lift force and torque coefficients for non-spherical particles in flows. *International Journal of Multiphase Flow*, 39:227–239, 2012.

[24]Rafik Ouchene, Mohammed Khalij, Boris Arcen, and Anne Tanière. A new set of correlations of drag, lift and torque coefficients for non-spherical particles and large reynolds numbers. *Powder Technology*, 303:33–43, 2016.

[25]Sathish KP Sanjeevi, JAM Kuipers, and Johan T Padding. Drag, lift and torque correlations for non-spherical particles from stokes limit to high reynolds numbers. *International Journal of Multiphase Flow*, 106:325–337, 2018.

[26]R Ouchene. Numerical simulation and modeling of the hydrodynamic forces and torque acting on individual oblate spheroids. *Physics of Fluids*, 32(7), 2020.

[27]Konstantin Fröhlich, Matthias Meinke, and Wolfgang Schröder. Correlations for inclined prolates based on highly resolved simulations. *Journal of Fluid Mechanics*, 901:A5, 2020.

[28]C Castang, Santiago Lain, and Martin Sommerfeld. Pressure center determination for regularly shaped non-spherical particles at intermediate reynolds number range. *International Journal of Multiphase Flow*, 137:103565, 2021.

[29]R Ouchene. On the orientation dependence of the pressure and frictional drag experienced by spheroids in creeping flow. *Physics of Fluids*, 36(5), 2024.

[30]Jingliang Wang, Lun Ma, Maoqiang Jiang, Qingyan Fang, Chungen Yin, Peng Tan, Cheng Zhang, and Gang Chen. Direct numerical simulation of the drag, lift, and torque coefficients of high aspect ratio biomass cylindrical particles. *Physics of Fluids*, 36(1), 2024.

[31]Greg A Voth and Alfredo Soldati. Anisotropic particles in turbulence. *Annual Review of Fluid Mechanics*, 49:249–276, 2017.

[32]Efstathios E Michaelides and Zhigang Feng. Drag coefficients of non-spherical and irregularly shaped particles. *Journal of Fluids Engineering*, 145(6):060801, 2023.

[33]Philip Geoffrey Saffman. The lift on a small sphere in a slow shear flow. *Journal of fluid mechanics*, 22(2):385–400, 1965.

[34]Shōichi Wakiya. Viscous flows past a spheroid. *Journal of the Physical Society of Japan*, 12(10):1130–1141, 1957.

[35]S Wakiya. Effect of a submerged object on a slow viscous flow (report v). spheroid at an arbitrary angle of attack. *Res. Rep. Fac. Engng Niigata Univ.(Japan)*, 8:17–30, 1959.

[36]Arthur Joseph Goldman, Raymond G Cox, and Howard Brenner. Slow viscous motion of a sphere parallel to a plane wall—i motion through a quiescent fluid. *Chemical engineering science*, 22(4):637–651, 1967.

[37]David Leighton and Andreas Acrivos. The lift on a small sphere touching a plane in the presence of a simple shear flow. *Zeitschrift für angewandte Mathematik und Physik ZAMP*, 36(1):174–178, 1985.

[38]ME O'neill. A sphere in contact with a plane wall in a slow linear shear flow. *Chemical Engineering Science*, 23(11):1293–1298, 1968.

[39]Lanying Zeng, Fady Najjar, S Balachandar, and Paul Fischer. Forces on a finite-sized particle located close to a wall in a linear shear flow. *Physics of fluids*, 21(3), 2009.

[40]TC Price. Slow linear shear flow past a hemispherical bump in a plane wall. *The Quarterly Journal of Mechanics and Applied Mathematics*, 38(1):93–104, 1985.

[41]AW El-Kareh and TW Secomb. Stokes flow impinging on a spherical cap on a plane wall. *The Quarterly Journal of Mechanics and Applied Mathematics*, 49(2):179–183, 1996.

[42]K Sugiyama and M Sbragaglia. Linear shear flow past a hemispherical droplet adhering to a solid surface. *Journal of engineering mathematics*, 62:35–50, 2008.

[43]R Martino, A Paterson, and M Piva. Onset of motion of a partly hidden cylinder in a laminar shear flow. *Physical Review E—Statistical, Nonlinear, and Soft Matter Physics*, 79(3):036315, 2009.

[44]Benjamin Boulbene, Jérôme Morchain, Muriel Mercier Bonin, Sébastien Janel, Frank Lafont, and Philippe Schmitz. A combined computational fluid dynamics (cfd) and experimental approach to quantify the adhesion force of bacterial cells attached to a plane surface. *AIChE journal*, 58(12):3614–3624, 2012.

[45]Samuel Musong, Zhi-Gang Feng, Kai Chen, and Quan-Wei Xu. Effects of rod shapes on the drag force of particles in a shear flow. In *ASME International Mechanical Engineering Congress and Exposition*, volume 46469, page V003T03A043. American Society of Mechanical Engineers, 2014.

[46]Sara Brambilla, Scott Speckart, and Michael J Brown. Adhesion and aerodynamic forces for the resuspension of non-spherical particles in outdoor environments. *Journal of Aerosol Science*, 112:52–67, 2017.

[47]Patrick Fillingham, Ravi S Vaddi, Andrew Bruning, Gunnar Israel, and Igor V Novosselov. Drag, lift, and torque on a prolate spheroid resting on a smooth surface in a linear shear flow. *Powder technology*, 377:958–965, 2021.

[48]Heng Zheng Ting, Pavel Bedrikovetsky, Zhao Feng Tian, and Themis Carageorgos. Impact of shape on particle detachment in linear shear flows. *Chemical Engineering Science*, 241:116658, 2021.

[49]George Gabriel Stokes et al. On the effect of the internal friction of fluids on the motion of pendulums. 1851.

[50]Mohammad Naghashnejad, Yen-Ting Lin, Elias Panides, Joy Banerjee, Seong H Kim, and Ali Borhan. Hydrodynamic force on a hemispheroidal particle attached to a planar surface in linear shear flow. *Powder Technology*, 434:119352, 2024.

[51]Atul Manikrao Bhagat and Partha Sarathi Goswami. Effect of rough wall on drag, lift, and torque on an ellipsoidal particle in a linear shear flow. *Physics of Fluids*, 34(8), 2022.

[52]Victor Chéron, Fabien Evrard, and Berend van Wachem. Drag, lift and torque correlations for axi-symmetric rod-like non-spherical particles in locally linear shear flows. *International Journal of Multiphase Flow*, 171:104692, 2024.

[53]Victor Chéron and Berend van Wachem. Drag, lift, and torque correlations for axi-symmetric rod-like non-spherical particles in linear wall-bounded shear flow. *arXiv preprint arXiv:2405.17124*, 2024.

[54]S Laín, C Castang, and M Sommerfeld. Study of flow resistance coefficients acting on regular non-spherical particles in simple shear flow at moderate reynolds numbers. *Powder Technology*, 435:119428, 2024.

[55]Kalyan Kottapalli and Igor V Novosselov. Experimental study of aerodynamic resuspension of rdx residue. *Aerosol Science and Technology*, 53(5):549–561, 2019.

[56]Ahad Zarghami and Johan T Padding. Drag, lift and torque acting on a two-dimensional non-spherical particle near a wall. *Advanced Powder Technology*, 29(6):1507–1517, 2018.

[57]SV Pantankar and Dudley Brian Spalding. *Mathematical models of fluid flow and heat transfer in furnaces: a review*. Imperial College [of Science and Technology], Mechanical Engineering Department, 1972.

[58]JJ Derksen and RA Larsen. Drag and lift forces on random assemblies of wall-attached spheres in low-reynolds-number shear flow. *Journal of Fluid Mechanics*, 673:548–573, 2011.

[59]Brian J O'Donnell and Brian Helenbrook. Drag on ellipsoids at finite reynolds numbers. *Atomization and Sprays*, 15(4), 2005.

[60]John Happel and Howard Brenner. *Low Reynolds number hydrodynamics: with special applications to particulate media*, volume 1. y Martinus Nijhoff Publishers, 1983.

[61]Sathish KP Sanjeevi and Johan T Padding. On the orientational dependence of drag experienced by spheroids. *Journal of Fluid Mechanics*, 820:R1, 2017.

[62]JR Agudo, C Illigmann, G Luzi, A Laukart, A Delgado, and A Wierschem. Shear-induced incipient motion of a single sphere on uniform substrates at low particle reynolds numbers. *Journal of Fluid Mechanics*, 825:284–314, 2017.